

## Wave-induced collisions of thin floating disks

L. J. Yiew, L. G. Bennetts, M. H. Meylan, G. A. Thomas, and B. J. French

Citation: *Physics of Fluids* **29**, 127102 (2017); doi: 10.1063/1.5003310

View online: <https://doi.org/10.1063/1.5003310>

View Table of Contents: <http://aip.scitation.org/toc/phf/29/12>

Published by the *American Institute of Physics*

---

### Articles you may be interested in

[Shapes and paths of an air bubble rising in quiescent liquids](#)

*Physics of Fluids* **29**, 122104 (2017); 10.1063/1.5006726

[Effect of surface roughness on droplet splashing](#)

*Physics of Fluids* **29**, 122105 (2017); 10.1063/1.5005990

[Introduction to Focus Issue: Two-Dimensional Turbulence](#)

*Physics of Fluids* **29**, 110901 (2017); 10.1063/1.5012997

[Interaction of wave with a body floating on a wide polynya](#)

*Physics of Fluids* **29**, 097104 (2017); 10.1063/1.4991675

[Lattice Boltzmann simulation of shear-induced particle migration in plane Couette-Poiseuille flow: Local ordering of suspension](#)

*Physics of Fluids* **29**, 121605 (2017); 10.1063/1.4991428

[Formation of liquid chain by collision of two laminar jets](#)

*Physics of Fluids* **29**, 112101 (2017); 10.1063/1.4998288

---



**COMPLETELY  
REDESIGNED!**

**PHYSICS  
TODAY**

*Physics Today* Buyer's Guide  
Search with a purpose.

## Wave-induced collisions of thin floating disks

L. J. Yiew,<sup>1,a)</sup> L. G. Bennetts,<sup>1</sup> M. H. Meylan,<sup>2</sup> G. A. Thomas,<sup>3,4</sup> and B. J. French<sup>4</sup>

<sup>1</sup>*School of Mathematical Sciences, University of Adelaide, Adelaide, SA 5005, Australia*

<sup>2</sup>*School of Mathematical and Physical Sciences, University of Newcastle, Callaghan, NSW 2308, Australia*

<sup>3</sup>*Department of Mechanical Engineering, University College London, London WC1E 7JE, United Kingdom*

<sup>4</sup>*National Centre for Maritime Engineering and Hydrodynamics, Australian Maritime College, Newnham, TAS 7248, Australia*

(Received 5 September 2017; accepted 22 November 2017; published online 14 December 2017)

Collisions between two thin floating disks forced by regular water waves are studied for a range of wave amplitudes and lengths, using laboratory wave basin experiments and a mathematical model. Three collision regimes are identified from the experiments in terms of collision frequency and strength, and the collisions are shown to be caused by drift for short incident wavelengths and relative surge motion between the disks for longer incident waves. The model is based on slope-sliding theory for the wave-induced disk motions and rigid-body collisions. It is shown to predict collision frequencies and velocities accurately for intermediate–long incident wavelengths. Incorporating drift and wave scattering forces into the model is shown to capture the collision behaviours for short incident wavelengths. *Published by AIP Publishing.* <https://doi.org/10.1063/1.5003310>

### I. INTRODUCTION

The outer tenths to hundredths of kilometres of the sea ice covered ocean is characterised by fields of relatively small floes (discrete, thin chunks of floating sea ice), separated by open water or a thin viscous layer of ice crystals (frazil or grease ice) and ice fragments (brash ice). Depending on the season and location, the floes can be small, thin disks of newly formed ice (known as pancake ice, with thicknesses of order 10 mm and radii of order 0.1 m–1 m) or larger, thicker, older chunks of fractured ice pushed out from the inner pack (thicknesses of order 0.1 m–1 m and horizontal dimensions of order 10 m–100 m). It is a highly dynamic region, with floes easily displaced by winds, by currents, and, of particular interest in this study, by surface gravity waves. Waves cause floes to drift in the direction of the waves and to oscillate at the wave period, both in the plane of the undisturbed floes (translational surge and sway, and rotational yaw) and out of plane (translational heave, and rotational pitch and roll).

At medium to high concentrations of ice cover, differential lateral motions of the floes—due to winds, currents, or waves—force floe–floe collisions. [Martin and Becker \(1987; 1988\)](#) reported accelerometer measurements of collisions in the Bering and Greenland Seas, identifying regular, minor collisions correlated to the local wave activity and sporadic, major events they attributed to large-scale deformation of the ice field. [Rottier \(1992\)](#) also reported accelerometer measurements of collisions from a later set of experiments in the Barents and Greenland Seas, similarly finding occurrence of collisions correlated to the local wave activity and observing that brash ice (likely produced by collisions) modifies collision rates.

Theoretical and numerical models of wave-induced collisions between floes have been developed to assess potential effects on dynamic and thermodynamic properties of the ice cover and on attenuation of wave energy. The floes are conventionally modeled as thin floating bodies, typically beams in 1D models and disks in 2D models. [McKenna and Crocker \(1990\)](#) modeled collisions between two floes (disks) due to regular (monochromatic and unidirectional) waves, assuming that floes simply follow the prescribed circular trajectories of surface water particles [implicitly assuming that wavelengths are much greater than floe diameters and the floes do not modify the wave field; see, e.g., [Masson and LeBlond \(1989\)](#)] and using the model to study wave attenuation and floe erosion caused by the collisions. [Gao \(1991\)](#) proposed a simple 1D collision criterion for neighbouring floes due to surge motion forced by regular waves, also based on the assumption that floes follow prescribed circular trajectories of water particles, and used this to derive predictions of collision frequencies in a large 2D field of floes, by treating floe motions and separation distances in the wave propagation direction as stochastic processes. He compared model predictions with data obtained from accelerometer measurements deployed on floes in the Labrador Sea, finding that his predictions differed from the accelerometer data by an order of magnitude.

[Shen and Ackley \(1991\)](#) developed a 1D model of collisions due to regular waves in a periodic field of floes and used it to study herding of floes. They modeled floe motions using slope-sliding theory ([Rumer et al., 1979](#); [Marchenko, 1999](#); and [Grotmaack and Meylan, 2006](#)), in which the floes surge back and forth and drift due to gravity pulling the floe down the moving wave profile. The floes do not modify the surrounding wave field, but follow different trajectories to the surface water particles, calculated as the solution of an ordinary differential equation. Collisions were modeled using a spring–dashpot model, in which floes are elastic bodies, and collisions are governed by spring and damping coefficients.

<sup>a)</sup>Author to whom correspondence should be addressed: lucas.yiew@ntu.edu.sg and lucas.yiew@gmail.com. Current address: Environmental Process Modelling Centre, Nanyang Environment & Water Research Institute, Nanyang Technological University, S637141 Singapore.

It was shown that prolonged contact of floes could be simulated with an appropriate damping coefficient, and it was suggested that under the right thermodynamic conditions, prolonged contact will lead to the formation of composite floes as they freeze together. Shen and Squire (1998) later used the model to study wave attenuation due to collisions.

Rottier (1992) modeled collisions in 2D (one horizontal dimension and one depth dimension) between two floes, due to surge motions induced by wave-driven hydrodynamic pressure on the submerged floe edges, where the floes are modeled as thin rigid bodies and also heave and pitch in response to wave forcing. He incorporated the random nature of the wave amplitude in the ocean and adopted the assumption that floes follow the trajectories of surface water particles. Brash ice was included in the model as a small rigid body between the floes and acted as an intermediary in the collision process. Rottier showed that the model provides reasonable agreement with his field measurements.

Models of collisions between floes driven by non-wave processes have also been developed. In a relevant recent series of studies, Herman (2011; 2012; 2013) numerically modeled in-plane motions of a field of thousands of colliding 2D floes (disks) with a distribution of sizes, forced by winds and currents. She used the model to study cluster formations and force/contact networks between floes.

Frankenstein (1996) used laboratory wave tank experiments to study collisions between floes forced by regular incident waves, for wavelengths much greater than the floe lengths (by at least an order of magnitude). One set of tests was conducted in a standard wave tank with up to four plastic plates in-line with the incident waves and for incident-wave steepnesses  $ka \approx 0.005\text{--}0.14$ , where  $k$  is the wavenumber and  $a$  is the wave amplitude. A second set of tests was conducted in a refrigerated tank with up to 50 floes formed from urea ice, for incident wave steepnesses  $ka \approx 0.03\text{--}0.1$ . She compared the collision frequencies and durations to predictions given by the model of Shen and Ackley (1991), finding generally poor agreement, which she attributed to sensitivities to initial conditions, experimental errors, and physical effects (specific to the design of the experiment) not included in the model, e.g., friction between floes and damping of lateral floe motions caused by a guide wire installed to prevent floes from rotating horizontally.

Bennetts and Williams (2015) reported accelerometer measurements of collisions between 80 identical thin wooden disks in a large wave basin, forced by regular incident waves with wavelengths ranging from approximately two-thirds of the disk diameter to six times the disk diameter and steepnesses  $ka \approx 0.04\text{--}0.26$ . They found that collisions were most forceful in the mid-wavelength regime and that for tests in this regime with large incident steepnesses, the collisions turn into rafting events. Moreover, they reported measurements of the wave field transmitted by the disks and noted greater wave attenuation in tests where strong, frequent collisions occurred.

The present investigation follows that of Yiew *et al.* (2016), who analysed laboratory experimental measurements of the oscillatory hydrodynamics (surge, heave, and pitch) of a solitary thin floating plastic disk, induced by regular

incident waves for wavelengths ranging from approximately equal to the disk diameter to over an order of magnitude greater than it and steepnesses  $ka \approx 0.01\text{--}0.3$ . They showed that a linear relationship exists between the incident-wave amplitude and surge, heave, and pitch motions. They also showed that slope-sliding theory predicts surge motions accurately for wavelengths greater than three times the disk diameter (i.e., relatively low frequency waves), and for shorter wavelengths (higher wave frequencies), linear potential-flow theory predicts disk hydrodynamics (surge, heave, and pitch) accurately.

Here, laboratory experiments are reported in which regular incident waves force motions of two identical disks in-line with the wave direction, causing the disks to collide for certain incident wavelengths and amplitudes. The same facility and disks are used as in the solitary-disk experiments reported by Yiew *et al.* (2016), and a subset of their incident-wave conditions is tested. The disks are moored to allow multiple collisions and have edge barriers attached as a simplifying measure to prevent rafting events. Methods are devised to identify collision events and collision velocities from non-contact measurements of the disk displacements. Three collision regimes, and the dominant physical mechanisms affecting their collision behaviours, are identified in terms of incident wavelength and amplitude. Collisions are shown to be forced by drift in the short incident wavelength regime and the relative surge motion between the disks for longer incident wavelengths.

Further, a mathematical model is developed, based on slope-sliding theory for the wave-induced disk motions [similar to Shen and Ackley (1991) and others] and rigid-body collisions [similar to Herman (2011; 2012; 2013)]. The model is shown to predict collision frequencies and velocities accurately for intermediate-long wavelengths. For short incident wavelengths, the model is extended to include drift and wave scattering forces, and this is shown to improve predictions of disk displacements and collision behaviours significantly. A subset of this investigation appears in the Ph.D. thesis of Yiew (2017).

## II. EXPERIMENTS

### A. Methods

Experiments investigating collisions between two identical, moored disks, forced by regular incident waves, were conducted in the model test basin (MTB) at the Australian Maritime College, Launceston, Australia. Figures 1 and 2 show a schematic plan view and photo of the experimental setup, respectively. The MTB is 35 m long and 12 m wide and was filled with fresh water of density  $\rho \approx 1000 \text{ kg m}^{-3}$  to depth  $h = 0.83 \text{ m}$ . A piston-type wave maker at the left-hand end of the MTB generated regular incident waves, and a sloping beach at the right-hand end reduced wave energy reflected from this boundary, with the reflected waves found to contain less than 2% of the incident energy. The disks were positioned in-line with the incident-wave direction and separated by  $s_0 = 20 \text{ mm}$  at their closest points. The left-hand disk (closest to the wave maker) is referred to as disk 1, and the right-hand disk (closest to the beach) is referred to as disk 2. With this setup, disk motions are essentially one-dimensional (left/right

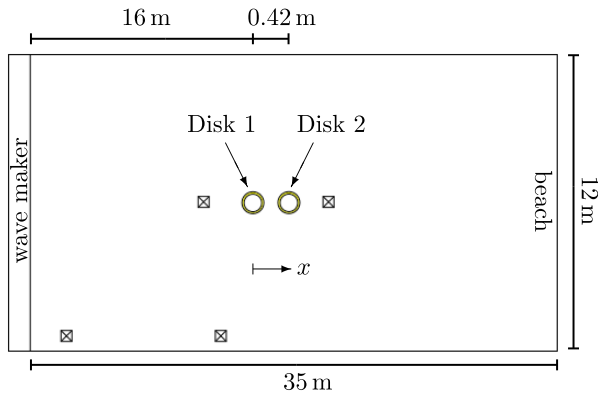


FIG. 1. Schematic plan view of the MTB and experimental setup (x symbols indicate wave probe locations).

with respect to Fig. 1), with lateral motions (up/down) not being excited. The coordinate  $x$  is assigned to the direction of the motions, pointing in the direction of incident-wave propagation, i.e., from left to right.

The disks are made of Nycel plastic (expanded rigid-foam PVC), with diameter  $D = 0.4$  m, thickness  $H = 15$  mm, density  $\approx 636$  kg m $^{-3}$ , and hence mass  $m \approx 1.2$  kg. As a simplifying measure, light-weight styrofoam edge barriers, 50 mm high and 25 mm thick, were installed on both disks to prevent rafting from occurring. The barriers also prevent waves from washing over the disks, which would reduce the surge response of individual disks to short-period waves (Bennetts and Williams, 2015 and Yiew *et al.*, 2016). Nylon wires were used to moor the disks to the sides of the MTB, in order to (i) limit the drift of the disks and keep them within a consistent field-of-view, (ii) reset the disks to their initial configurations after each test, and (iii) allow for multiple collisions during individual tests, in order to minimise variability in the mean collision properties between repeated tests.

Following Yiew *et al.* (2016), who used a similar experimental setup, four light-weight tracking balls/markers were attached to each disk via aluminium rods, as shown in Fig. 2. The combined mass of the tracking balls, rods, and barrier for each disk was 0.06 kg or  $\approx 5\%$  of the disk's mass. The effect of these objects on disk motions is assumed to be negligible, noting that Yiew *et al.* (2016) found good agreement between measured surge, heave, and pitch motions and model predictions. Further, Meylan *et al.* (2015a) and Montiel *et al.* (2013a; 2013b) used  $\geq 4$  times as many markers to measure the hydroelastic behaviour of thin compliant floating bodies and

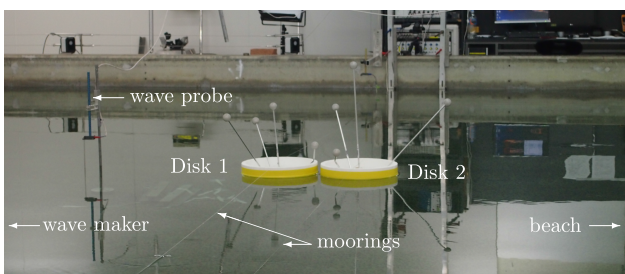


FIG. 2. Photo of experimental setup in initial configuration.

did not report that the markers had any significant influence on rigid-body and flexural responses.

Marker locations during the tests were recorded by the Qualisys non-contact motion-tracking system, which consists of eight pairs of infrared cameras and receivers installed along the perimeter of the wave basin. The heights of the markers were carefully tuned so that the Qualisys system could differentiate the different disks, and the locations of the markers were restricted so that they would not overlap/collide when the disks were close together. Motions were recorded over 60.24 s at a frame rate of 200 Hz.

Tests were conducted for incident-wave frequencies  $f = 0.5$ – $1.5$  Hz, giving incident wavelengths,  $\lambda$ , ranging from comparable to the disk diameter,  $\lambda/D \approx 1.7$  for  $f = 1.5$  Hz, to over an order of magnitude greater than the diameter,  $\lambda/D \approx 12.3$  for  $f = 0.5$  Hz. For each frequency, three target wave amplitudes were tested,  $a = 10$  mm, 20 mm, and 40 mm, giving wave steepnesses,  $ka$ , where  $k = 2\pi/\lambda$  is the wave number, ranging from mild,  $ka \approx 0.013$  for  $f = 0.5$  Hz and  $a = 10$  mm, to storm-like,  $ka \approx 0.314$  for  $f = 1.4$  Hz and  $a = 40$  mm. (Weakly nonlinear waves—defined by sharp peaks and rounded troughs—were visually observed to develop when  $ka > 0.21$ , approximately.) Table I summarises the tests considered, noting that for  $a = 40$  mm the tests with  $f = 1.2$  and 1.5 Hz are not analysed, due to data acquisition issues for  $f = 1.2$  Hz and the large incident-wave steepness for  $f = 1.5$  Hz ( $ka \approx 0.364$ ) causing significant wave breaking and wave spilling over the edge barrier.

Four wave probes were used to measure wave elevations around the MTB, as shown in Fig. 1. Two probes were installed along the sides of the basin, with one measuring the wave field close to the wave maker and the other measuring the wave field approximately 15 m down the wave basin. The other two probes were positioned approximately 2 m in front of disk 1 and 2 m behind disk 2. Measured wave frequencies were consistent with target frequencies, with the largest difference less than 2% of the target value. Measured wave amplitudes were smaller than target values, with amplitudes in front of disk 1 on average 14% smaller than target amplitudes; consequently  $a_m$  is used to denote the measured amplitude in the results where necessary.

Overall, 62 tests (inclusive of 39 repeated tests) were conducted, and data from 47 of these tests were analysed. The tests not analysed were deemed unsuccessful due to (i) data acquisition errors (also noted above) resulting from markers merging on the IR image and (ii) strong drift causing disk 2 to collide with the wave probe behind it (in which case the wave probes were repositioned and tests repeated). All tests were recorded by a video camera from the side of the MTB and approximately level with the disks, in order to perform an initial qualitative assessment of the collision behaviours.

TABLE I. Incident-wave properties for tests analysed.

$f$ (Hz)	0.5	0.75	1	1.1	1.2	1.3	1.4	1.5
$\lambda$ (m)	4.91	2.67	1.56	1.29	1.08	0.92	0.8	0.69
$a = 10$ mm	•	•	•	•	•	•	•	•
$a = 20$ mm	•	•	•	•	•	•	•	•
$a = 40$ mm	•	•	•	•		•	•	

## B. Surge and drift

The longitudinal disk motions (i.e., in the  $x$ -direction) that drive collisions are combinations of surge and drift. Surge is the oscillatory back-and-forth motion at the frequency of the incident wave, and drift is the net displacement along the MTB (in the positive  $x$ -direction).

Figure 3(a) shows surge response amplitude operators (RAOs),

$$A_{\text{surge}} = \frac{a_{\text{surge}} \tanh(kh)}{a_m}, \quad (1)$$

where  $a_{\text{surge}}$  is the surge amplitude, as functions of non-dimensional incident wavelength,  $\lambda/D$ . The surge amplitudes are calculated from the  $x$ -locations of the disks provided by Qualisys, during a 30 s steady-state interval following the initial transient motions. The discrete Fourier transform of each signal is calculated using the MATLAB `fft` function, to produce the frequency spectrum of the signal, and the surge amplitude is identified as the local maximum amplitude closest to the incident-wave frequency. Mean values of the surge RAOs with respect to incident amplitudes are shown, along with error bars that indicate the RAO range. The results of Yiew *et al.* (2016) for a solitary disk (with an edge barrier) are overlaid for comparison, including a trend line [i.e., a best-fit polynomial curve, see Yiew (2017), Sec. 2.3.1] and noting that the mooring used in the solitary-disk tests was far looser than used in the two-disk tests.

Surge RAOs for the two disks are consistent with the solitary-disk RAO, with mean values within 4.6% of the solitary-disk trend line. This implies that the different mooring system used in the collision experiments does not affect the surge motions and that the disks do not affect each others' surge motions. The RAOs increase rapidly with increasing wavelength for short incident wavelengths, from  $A_{\text{surge}} \approx 0.62$  at  $\lambda/D = 1.72$  to  $\approx 0.87$  at  $\lambda/D = 2.7$ , followed by more modest increases for  $2.7 < \lambda/D < 6.7$ , before settling to an approximately unitary value for  $\lambda/D > 6.7$ . Further, Yiew *et al.* (2016)

reported comparable surge amplitudes for a solitary disk in free drift and under the influence of a mooring line (see Sec. 2.2). Based on their findings, it can be inferred that the mooring system used in the two-disk tests does not influence surge motions of the disks.

Figure 3(b) shows the drift velocity,  $v_{\text{drift}}$ , of a solitary disk [noting Yiew *et al.* (2016) did not report drift measurements], in comparison to cognate wave tank measurements reported by Huang *et al.* (2011) and McGovern and Bai (2014). Following these authors,  $v_{\text{drift}}$  is normalised with respect to wave celerity,  $c_p = f\lambda = 2\pi f/k$ , and shown as a function of wave steepness. The drift velocity of the disk is calculated as the maximum velocity during the free-drift interval [beginning after the initial transient phase and ending when the tether engages, see Yiew (2017), Sec. 2.3.2 for details]. Data are grouped according to target incident-wave amplitude, and trend lines proportional to  $(ka_m)^2$  (similar to Stokes drift) are overlaid.

Huang *et al.* (2011) measured drift velocities of paraffin wax plates for incident-wave steepnesses  $ka = 0.04$ – $0.15$  and non-dimensional incident wavelengths  $\lambda/D_l = 6.3$ – $7.8$ , where  $D_l$  denotes the plate length in the direction of the incident wave. Figure 3(b) shows data for a square plate of thickness to length quotient 0.225 and mass 1.7 kg, i.e., an order of magnitude thicker than the Nycel disk and  $\approx 40\%$  heavier. McGovern and Bai (2014) measured drift velocities of plastic (polyethylene) plates for incident-wave steepnesses  $ka = 0.02$ – $0.31$ , and non-dimensional wavelengths  $\lambda/D_l = 1.3$ – $10$ . Data shown are again for a square plate, in this case with thickness to length quotient 0.167 and mass 4 kg, i.e., an order of magnitude thicker than the Nycel disk and  $>300\%$  heavier. McGovern and Bai also measured the drift velocities of triangular and rectangular plates (not shown) of similar lengths and thicknesses but found that the different shapes did not affect drift significantly. They noted that their measured drift velocities were approximately equal to Stokes drift velocity [overlaid in Fig. 3(b)], whereas Huang *et al.* noted that their measured drift velocities were greater than Stokes drift

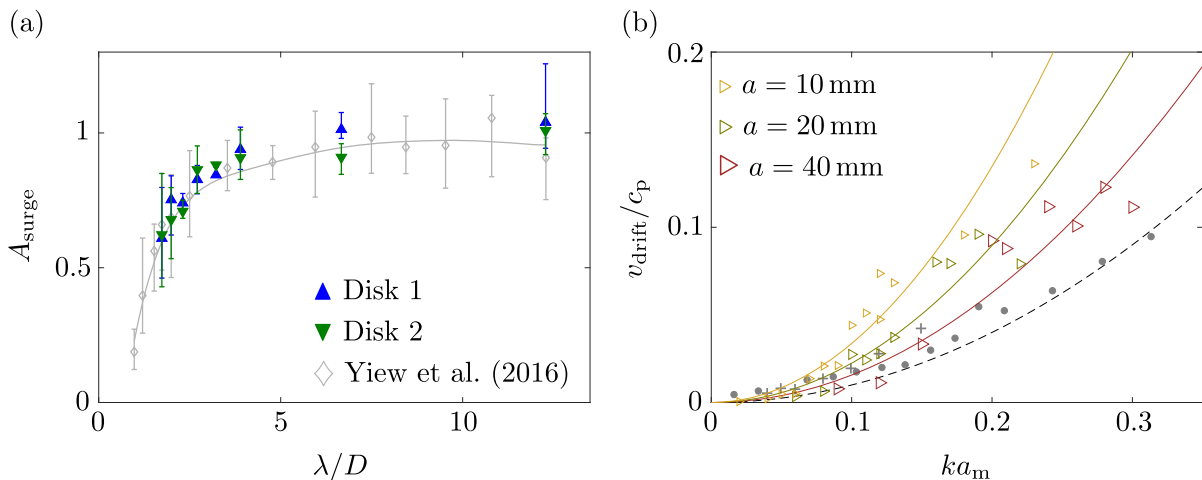


FIG. 3. (a) Mean surge RAOs of disk 1 (blue-filled triangles) and disk 2 (green-filled inverted triangles), with respect to incident amplitude, as functions of non-dimensional incident wavelength, with error bars showing the ranges. Corresponding surge RAO measurements for a solitary disk (gray diamond) are overlaid, including error bars and trend lines [from Yiew *et al.* (2016)]. (b) Normalised drift velocities of a solitary disk as a function of incident-wave steepness, with velocities grouped according to  $a = 10$  mm (gold triangles), 20 mm (olive green triangles), and 40 mm (maroon triangles), and corresponding trend lines provided. Measurements of McGovern and Bai (2014) (gray dots) and Huang *et al.* (2011) (gray crosses) of drift velocity are overlaid, along with Stokes drift velocity (---).

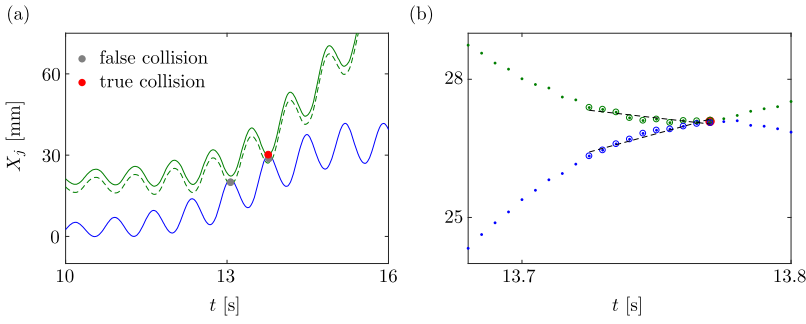


FIG. 4. (a) Signals for disk 1 (blue curve) and disk 2 (green dashed curve), resulting in two erroneously identified collision events (gray bullets) due to disk separations being too small. Moving disk 2 back  $\varepsilon = 3$  mm (green curve) identifies the single true collision event (red bullet). (b) Discrete locations of disk 1 (blue dots) and disk 2 (green dots) around a collision event (red bullet). The 10 locations leading up to the collision are encircled, and linear regression lines (--) are superimposed, from which the disk velocities are calculated as the slopes.

velocity, with the difference increasing as the incident steepness increases.

Consistent with the findings of Huang *et al.* (2011) and McGovern and Bai (2014), the normalised drift velocities of the Nycel disk generally increase as incident-wave steepness increases, i.e., incident amplitude increases and/or wavelength decreases. The drift velocities of the disk significantly exceed those of the square plates, particularly for  $ka > 0.1$ , which is attributed to the disk being lighter than the square plates. For a given incident steepness,  $ka_m = 2\pi a_m/\lambda$ , the drift velocity of the disk decreases as incident amplitude,  $a_m$ , increases, indicating that drift velocity is more sensitive to incident amplitude than wavelength.

### C. Collision detection

Let  $x = X_1(t)$  denote the position of the geometric centre of disk 1 provided by Qualisys measurements and  $x = X_2(t)$  denote the position of disk 2. The instantaneous separation distance of the disks is defined as

$$s(t) = X_{1,r}(t) - X_{2,f}(t), \quad (2)$$

where  $X_{1,r}(t) = X_1(t) + D/2$  and  $X_{2,f}(t) = X_2(t) - D/2$  are the positions of the rearmost point of disk 1 and the frontmost point of disk 2, respectively, i.e., the disks' closest points. This definition assumes that the disks remain in-plane, neglecting heave and pitch (the out-of-plane motions), noting that for the steepest waves reported,  $ka \approx 0.314$ , the maximum pitch angle is  $17.4^\circ$ , and the in-plane definition of the closest points is within 5% of the actual  $x$ -coordinates of the disks at their rearmost and frontmost points, respectively.

For tests in which collisions were observed, collision times are provisionally identified as the times at which  $s(t) \leq 0$ . This method misses some collisions, erroneously identifies others, and identifies multiple collision times for the same collision event, due to (i) the in-plane approximation of the disk edges, (ii) small discrepancies in the initial separations of the disks, and (iii) noise in the Qualisys signals. The separation distance signal for each test in which collisions occur is shifted by a small value of  $\varepsilon$  to identify collisions correctly, and collisions within a 2 s radius interval are merged to identify a unique collision time for each collision. The number of collision events is confirmed using the video recordings.

Figure 4(a) shows an example of two falsely acquired collision events, due to separation distances being too small. The single true collision in this time interval, which occurs fractionally before the second false collision, is identified using

$\varepsilon = 3$  mm, which is illustrated by moving disk 2 slightly away from disk 1.

For each collision, a collision velocity,  $V_{\text{col}}$ , is defined as

$$V_{\text{col}} = \frac{1}{2}|V_1 - V_2|, \quad (3)$$

where  $V_1$  and  $V_2$  are the velocities of disks 1 and 2, respectively, going into the collision. The disk velocities are calculated as the slope of a linear regression of the  $x$ -signal over the 10 time steps leading up to the collision, as illustrated in Fig. 4(b).

### D. Collision regimes

Three distinct collision behaviours were observed during the tests:

- (I) the disks do not collide during a given test;
- (II) they collide repeatedly at regular time intervals;
- (III) they collide 1–3 times during the initial phase of their motions.

Figure 5 shows the collision behaviours displayed in each test, as a function of non-dimensional incident amplitude,  $a_m/s_0$  (recalling that  $s_0$  is the initial separation), and wavelength,  $\lambda/D$ . Underlying colours are used to divide amplitude–wavelength space into regimes corresponding to

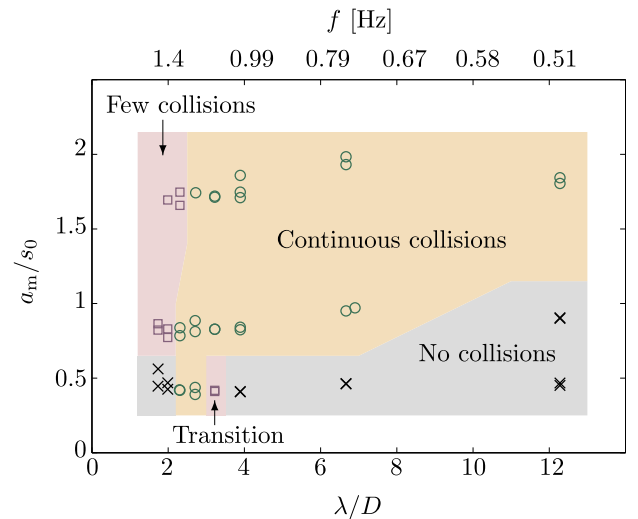


FIG. 5. Collision behaviours in non-dimensional incident-wave amplitude–wavelength space: behaviour I (no collisions, black crosses); II (regular collisions, green circles); and III (1–3 collisions, purple squares). Underlying colours divide amplitude–wavelength space into different collision behaviours.

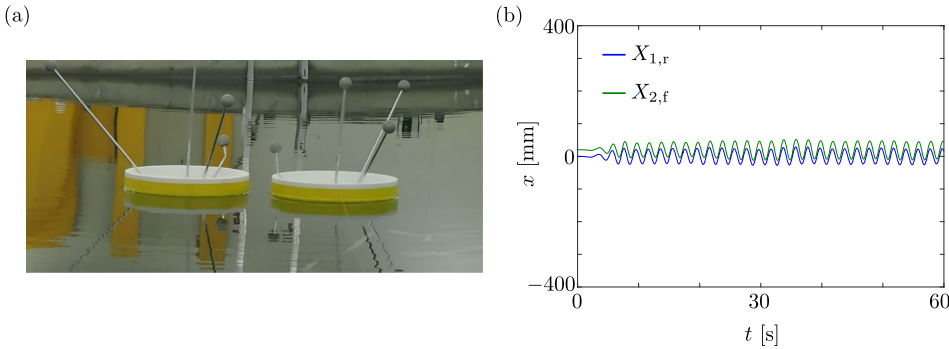


FIG. 6. (a) Photo and video and (b) measured disk displacements (disk 1 rear,  $X_{1,r}$ , blue curve; and disk 2 front,  $X_{2,f}$ , green curve) for a test giving behaviour I, with  $\lambda/D = 12.3$  ( $f = 0.5$  Hz) and  $a/s_0 = 1$ . Multimedia view: <https://doi.org/10.1063/1.5003310.1>

behaviours I–III. Incident amplitudes are non-dimensionalised with respect to  $s_0$ , as the magnitude of  $a_{\text{surge}} [\approx a_m$  in long waves; see Fig. 3(a)] in comparison to  $s_0$  dictates the likelihood of collisions due to surge, in the absence of phase considerations.

Behaviour I occurs for both small and large incident wavelengths and small amplitudes but increases to moderate amplitudes for the longest wavelengths tested. Wave steepnesses in this regime range from small to moderate, with  $ka_m = 0.067$ – $1.016$  in the short-wavelength, no-collision regime ( $\lambda/D \leq 1.99$ ) and  $ka_m = 0.013$ – $0.033$  for the longer-wavelength regime ( $\lambda/D \geq 3.89$ ). Figure 6 (Multimedia view) shows a photo, video, and  $x$ -motions of the disks from a test with  $\lambda/D = 12.3$  and  $a/s_0 = 1$ . The disk motions are dominated by surge and are almost identical, with only a small phase separation. The surge amplitudes are large enough to cause the range of  $x$ -locations occupied by the disks to overlap, but the disks are close enough to being in-phase with one another that they remain apart during their motion.

Behaviour II occurs for intermediate to long incident wavelengths and small to large amplitudes, with wave

steepnesses ranging from moderate to large:  $ka_m = 0.044$ – $0.201$ . Figure 7 (Multimedia view) shows a photo, video, and  $x$ -motions for a test in this regime, with  $\lambda/D = 2.7$  and  $a/s_0 = 1$ . Out-of-phase surge motions induced by the initial transients in the incident field drive the initial collision, causing the disks to rebound away from each other, until the mooring system pulls them back together, resulting in a second collision. This process repeats, with collisions every  $\sim 6.6$  s, and the collisions becoming stronger before settling to a regular pattern after the third collision. The collisions are relatively forceful, with mean collision velocities  $\approx 150 \text{ mm s}^{-1}$ .

Behaviour III occurs for small incident wavelengths and moderate to large amplitudes. Wave steepnesses in this regime are generally larger than the other regimes, with  $ka_m = 0.122$ – $0.267$ . Figure 8 (Multimedia view) shows an example from this regime, for the test in which  $\lambda/D = 1.7$  and  $a/s_0 = 1$ . The single, relatively weak (velocity  $\approx 60 \text{ mm s}^{-1}$ ) collision occurring in this test results from the initial transients in the incident field reaching disk 1 before disk 2, causing disk 1 to drift into disk 2. The drift force on disk 1 is strong enough to quickly overcome the rebound force (before the mooring engages) so that both

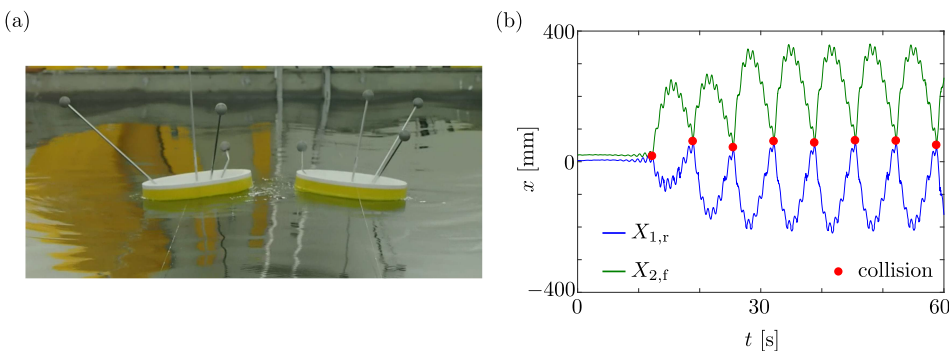


FIG. 7. (a) Photo and video and (b) measured disk displacements for a test giving behaviour II, with  $\lambda/D = 2.7$  ( $f = 1.2$  Hz) and  $a/s_0 = 1$ . Multimedia view: <https://doi.org/10.1063/1.5003310.2>

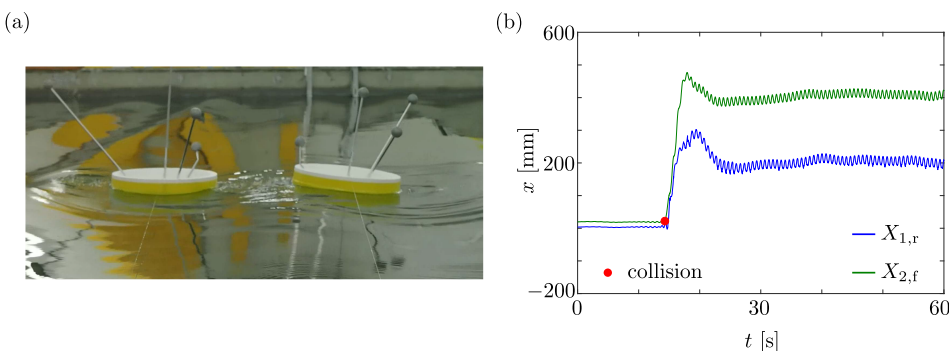


FIG. 8. (a) Photo and video and (b) measured disk displacements for a test giving behaviour III, with  $\lambda/D = 1.7$  ( $f = 1.5$  Hz) and  $a/s_0 = 1$ . Multimedia view: <https://doi.org/10.1063/1.5003310.3>

disks move down the MTB following the collision. Mooring of disk 2 prevents it from drifting beyond  $x \approx 480$  mm, and soon after the mooring engages, the disks settle to surging around a constant separation of 200 mm. This separation is an order of magnitude greater than the initial separation and was visibly due to scattered wave forces between the disks. For smaller incident amplitudes, the drift force is not strong enough to force a collision during the time lag for the disks beginning to drift.

Figure 5 also shows two transitory tests at  $\lambda/D = 3.2$  and  $a_m/s_0 = 0.41$ . In these tests, solitary, very weak collisions (velocity  $\approx 10$ – $14$  mm  $s^{-1}$ ) occurred at early times during the tests. For the remainder of the tests, the disks surged approximately in phase with one another, similar to the motions shown in Fig. 6(b). These tests are classified as behaviour III, although they actually indicate the transition from regular collisions (behaviour II), due to significant out-of-phase surge motions, to no collisions (behaviour I), due to in-phase surge motions, as incident wavelength increases, for the smallest target amplitudes,  $a/s_0 = 0.5$ .

### E. Relative surge

Figure 9(a) shows the relative surge of the disks,

$$\Delta\text{Surge} = \left| \bar{a}_{\text{surge}}(e^{i\varphi_1} - e^{i\varphi_2}) \right|, \quad (4)$$

where  $\bar{a}_{\text{surge}}$  is the mean surge amplitude with respect to the two disks, and  $\varphi_1$  and  $\varphi_2$  represent the phases of  $x$ -displacement of disks 1 and 2, respectively, as a function of non-dimensional incident wavelength, with the collision behaviours indicated, as in Fig. 5. For tests in which collisions occurred, the phases are calculated as  $\varphi_j = 2\pi f t_{\text{max},j}$ , where  $t_{\text{max},j}$  is the time disk  $j$  experiences its local maximum  $x$ -displacement prior to the first collision event (phases typically change following a collision). For tests in which collisions did not occur, the phases were calculated using the mean phases of all local maxima within the steady-state interval. Periods between successive local maxima were, in general, consistent and varied by less than 2.5%.

The relative surge measures the maximum distance surge moves the disks towards one another. A relative surge value greater than or equal to the initial separation,  $\Delta\text{Surge}/s_0 \geq 1$ , indicates that surge will force collisions. Sufficiently large values require large surge amplitudes and out-of-phase surge motions. Figure 9(a) shows that tests in which initial collisions were observed to be driven by surge (behaviour II, green circles) satisfy  $\Delta\text{Surge}/s_0 \geq 1$ . Tests in which no collisions occur

(behaviour I, black crosses) satisfy  $\Delta\text{Surge}/s_0 < 1$ . Tests in which initial collisions were observed to be driven by differential drift (behaviour III, purple squares), i.e., collisions were not due to surge, have relative surge values both sides of unity [dashed line in Fig. 9(a)]. These observations suggest that (i) relative surge determines the occurrence of collisions in the regimes defined by behaviours I and II, which generally occur in intermediate to long wavelengths, and (ii) relative surge cannot be used to predict collisions in regimes where collisions are caused by differential drift.

Figure 9(b) is similar to Fig. 9(a) but shows relative surge values calculated using: (i) corresponding surge amplitudes from solitary-disk tests of Yiew *et al.* (2016) [using the trend line shown in Fig. 3(a)], and (ii) theoretical phase differences  $\varphi_2 - \varphi_1 = k(D + s_0)$ , i.e., the incident-wave phase change between initial disk locations. The tests in which initial collisions are driven by surge still satisfy  $\Delta\text{Surge}/s_0 \geq 1$ , and tests in which no collisions occurred still satisfy  $\Delta\text{Surge}/s_0 < 1$ . This implies that knowledge of the surge motion of a solitary disk is sufficient to predict surge-driven collisions of adjacent disks.

## III. MATHEMATICAL MODEL

### A. Equation of motion: Slope-sliding theory

In the absence of collisions, the horizontal motions of the individual disks are modeled using the nonlinear ordinary differential equation

$$m(1 + c_m) \frac{d^2 X_j}{dt^2} = -mg \left[ \frac{\partial \eta}{\partial x} \right]_{x=X_j} + \rho c_d W |\widehat{V}_j| \widehat{V}_j - K \check{X}_j - CV_j \quad \text{for } j = 1, 2. \quad (5)$$

The left-hand side of Eq. (5) represents the inertial force, where  $c_m$  is the added mass of disk  $j$ , i.e., its increased resistance to motion due to contact with water. The first term on the right-hand side is the gravitational sliding force, in which

$$\eta(x, t) = \hat{a} \sin(kx - \omega t) \quad (6)$$

is the linear (sinusoidal) wave profile ( $\hat{a}$  is defined below), setting the phase to zero without loss of generality. The second term is the drag force, representing the resistance between the water and disk, where  $W = \pi R^2$  is the wetted surface of disk  $j$ , and  $\widehat{V}(t) = V_w(t) - V(t)$  is the relative velocity of disk  $j$  to the velocity of the water particle on the water surface beneath it,

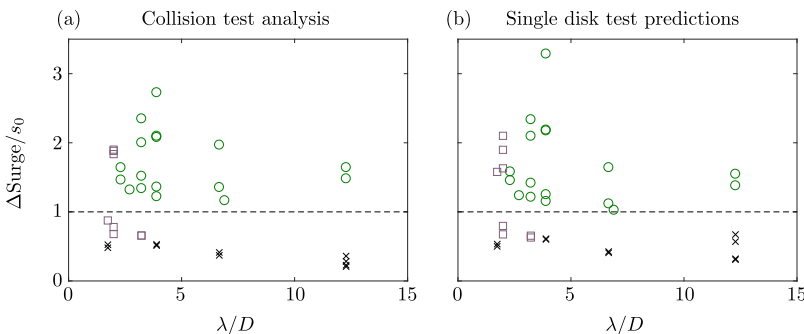


FIG. 9. Non-dimensional relative surge as a function of non-dimensional wavelength, with symbols denoting collision behaviours (as in Fig. 5) and dashed line (--) denoting relative surge equal to initial disk separation. (a) Relative surge values calculated from the collision tests. (b) Relative surge values calculated using surge amplitudes from solitary-disk tests and theoretical phase differences.

where

$$V_j = \frac{dX_j}{dt} \quad (7a)$$

is the velocity of disk  $j$ , and

$$V_w = \omega \hat{a} \sin(kX_j - \omega t) \coth kh \quad (7b)$$

is the velocity of the water particle. The third and fourth terms are, respectively, spring and damping forces applied by the mooring system, where  $K$  is the spring constant,  $\tilde{X}_j(t) = X_j(t) - X(0)$  is the displacement of disk  $j$  from its initial position, and  $C$  denotes the damping constant. Yiew *et al.* (2016) showed that Eq. (5), without the mooring terms, predicts the surge RAO of a solitary disk accurately when incident wavelengths are approximately three times greater than the disk diameter ( $f < 1.14$  Hz), for  $c_m = 0.1$  and  $c_d = 0$ , noting that Meylan *et al.* (2015b) had earlier shown that the RAOs are insensitive to the value of the drag coefficient.

Transients in the incident wave field are modeled to capture the initial collisions, which have different properties to those in the steady-state interval occurring in certain tests, as shown in Sec. II D. Therefore, the wave profile,  $\eta$ , is partitioned into a transient phase and a steady-state phase, using the envelope  $\hat{a}(x, t)$ , where  $\hat{a} = \alpha t^\beta$  during the transient phase ( $0 \leq t \leq t_s$ ) and  $\hat{a} = a_m$  during the steady phase ( $t > t_s$ ). The values of  $\alpha$ ,  $\beta$ , and  $t_s$  are obtained for each test by fitting Eq. (6) to data from the wave probe closest to disk 1 (with appropriate time offsets), using the `fit` function in MATLAB.

Spring and damping constants,  $K$  and  $C$ , are tuned by comparing horizontal disk motions in model simulations with measured motions from tests in which no collisions occurred, as translations experienced following a collision significantly complicate the tuning process. Thus, the mooring coefficients were tuned using a total of six tests, and the values  $K = 0.32 \pm 0.05$  and  $C = 0.5 \pm 0.1$  were found to give sufficient accuracy.

## B. Collisions

Equation (5) is solved for each disk at discrete time steps using the MATLAB function `ode45` (a variable step size fourth and fifth order Runge-Kutta integration method), with initial conditions

$$X_1(0) = 0, \quad X_2(0) = 420 \text{ mm}, \quad \text{and} \quad V_j(0) = 0 \quad (8)$$

for  $j = 1, 2$ . At the end of each time step, collisions are determined using the separation distance  $s$ , defined in Eq. (2), where the rearmost point of disk 1 and the frontmost point of disk 2 are calculated as

$$X_{1,r}(t) = X_1(t) + \frac{D}{2\sqrt{1 + \tan^2 \Theta_1(t)}} \quad (9a)$$

and

$$X_{2,f}(t) = X_2(t) - \frac{D}{2\sqrt{1 + \tan^2 \Theta_2(t)}}, \quad (9b)$$

respectively. Here,  $\Theta_1(t)$  and  $\Theta_2(t)$  denote the instantaneous pitch angles of disks 1 and 2, respectively, which are assumed to coincide with the angle of slope of the wave profile with respect to the positive horizontal direction, i.e.,

$$\Theta_j(t) = \arctan \left[ \frac{\partial \eta}{\partial x} \right]_{x=X_j(t)} \quad \text{for} \quad j = 1, 2. \quad (10)$$

For the purposes of modeling in-plane (non-rafting) collisions, disks are visualised as one-dimensional horizontal planes with no thicknesses. A collision event is defined to occur when the edges of the disks overlap, i.e., when  $X_{1,r} - X_{2,f} \geq 0$ .

Following Herman (2011; 2012; 2013), post-collision velocities of the disks are calculated using the principle of conservation of linear momentum and the restitution equation. Conservation of momentum gives the condition

$$m(V_{1,\text{col}+} + V_{2,\text{col}+}) = m(V_{1,\text{col}-} + V_{2,\text{col}-}), \quad (11a)$$

where  $V_{j,\text{col}\pm}$  denotes the velocity of disk  $j$  pre (–) and post (+) collision. The restitution equation is

$$\epsilon = \frac{V_{2,\text{col}+} - V_{1,\text{col}+}}{V_{1,\text{col}-} - V_{2,\text{col}-}}, \quad (11b)$$

where  $\epsilon$  is the restitution coefficient, with  $\epsilon = 0$  and 1 denoting perfectly inelastic and elastic collisions, respectively. Post-collision velocities are calculated in terms of the pre-collision velocities from Eqs. (11) as

$$V_{1,\text{col}+} = \frac{(1 - \epsilon)V_{1,\text{col}-} + (1 + \epsilon)V_{2,\text{col}-}}{2} \quad (12a)$$

and

$$V_{2,\text{col}+} = \frac{(1 + \epsilon)V_{1,\text{col}-} + (1 - \epsilon)V_{2,\text{col}-}}{2}. \quad (12b)$$

Tests showed that modeling the collisions as perfectly elastic ( $\epsilon = 1$ ) gives sufficiently accurate agreement with the experimental data. Under this condition, Eqs. (12) reduces to  $V_{1,\text{col}+} = V_{2,\text{col}-}$  and  $V_{2,\text{col}+} = V_{1,\text{col}-}$  [see Yiew (2017) for details].

The post-collision velocities are used as new initial conditions for the equations of motion to simulate post-collision displacements of the disks. The algorithm is repeated until another collision event occurs or if no more collisions occur after a prolonged period.

## C. Drag

The drag term in Eq. (5) becomes important when the disks move at relatively high velocities following a collision, with its value determining the maximum separation of the disks and the velocities at which they are pulled back towards one another by the moorings. For tests in which multiple collisions occur, the drag coefficient is tuned to give agreement between model predictions and experimental measurements with respect to disk displacements between collisions.

Figures 10(a) and 10(b) show model predictions of disk displacements overlaid on experimental measurements for a test with regular collisions (behaviour II;  $\lambda/D = 3.9$  and  $a/s_0 = 1$ ), with mean collision frequency  $\bar{f}_{\text{col}} = 0.143$  Hz (the reciprocal of the mean period between collisions, 6.99 s). Figure 10(a) shows predictions with  $c_d = 0.05$ , for which the model overpredicts the mean collision frequency to be  $\bar{f}_{\text{col}} = 0.125$  Hz (collisions every 8 s) and underpredicts the maximum disk separations following collisions. Figure 10(b) shows predictions with  $c_d = 0.005$ , for which the model predicts the mean collision frequency and maximum post-collision separations accurately (both within 1%) despite slight overpredictions of every other separation.

Figure 10(c) shows the drag coefficient as a function of incident-wave frequency and grouped according to target incident amplitudes. The drag coefficient tends to increase

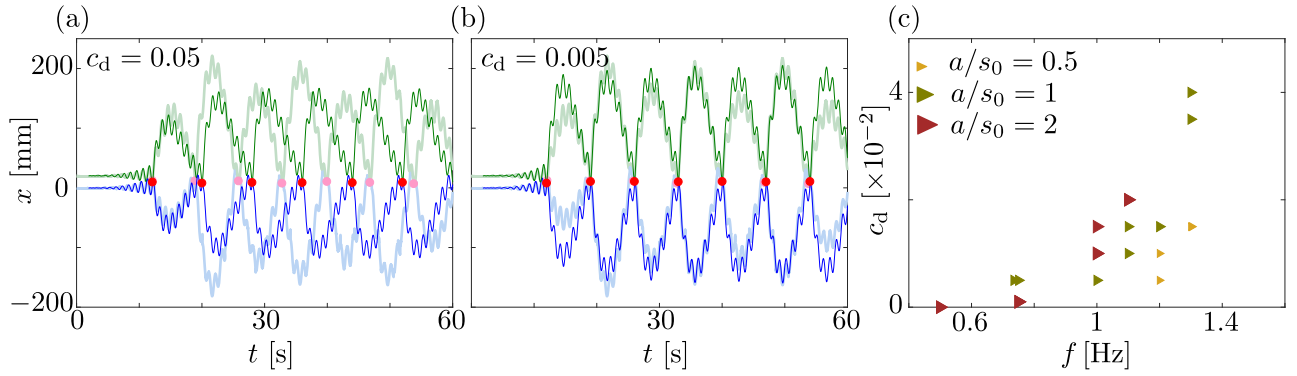


FIG. 10. (a) and (b) Disk displacements and collisions for  $\lambda/D = 3.9$  and  $a/s_0 = 1$ , predicted by model ( $X_{1,r}$ , blue curves;  $X_{2,f}$ , green curves; collision, red bullets) and measured during experiment (corresponding shaded curves and bullets). (c) Parameterised drag coefficient as a function of incident-wave frequency and grouped according to target incident-wave amplitude [symbols and colours as in Fig. 3(b)].

relatively weakly with increasing amplitude, with increases of factor  $\sim 3$  at a given frequency. It increases more strongly with increasing incident frequency, with order of magnitude increases over the frequency range considered for each amplitude group. The increases are attributed to greater pitching motion as frequency and amplitude increase, resulting in a greater form of drag.

#### IV. COLLISION FREQUENCIES AND VELOCITIES

Figure 11 shows model predictions and experimental measurements of the mean collision frequency,  $\overline{f_{\text{col}}}$ , and the corresponding mean collision velocity,  $\overline{V_{\text{col}}}$ , as functions of incident-wave frequency/non-dimensional wavelength and grouped according to the target incident-wave amplitude. The individual collision velocities,  $V_{\text{col}}$ , are calculated as outlined in Sec. II C for the experimental data, and

$$V_{\text{col}} = \frac{1}{2} |V_{1,\text{col}} - V_{2,\text{col}}| \quad (13)$$

for the model outputs. The experimental data shown are averaged with respect to repeated tests, and the collision frequency is set to zero for tests/simulations in which only a single collision occurred.

#### A. Experimental results

As indicated in Fig. 5, the mean collision frequencies calculated from the experimental data show that multiple collisions occur ( $\overline{f_{\text{col}}} \neq 0$ ) predominantly for mid-range frequencies, with the frequency range becoming wider as the incident amplitude increases. For the smallest amplitude,  $a/s_0 = 0.5$ , multiple collisions occur for frequencies  $f = 1.2$  and  $1.3$  Hz only ( $\lambda/D = 3.2$  and  $2.7$ ). These tests display behaviour II: regular, relatively strong collisions, with collision frequencies dictated by the moorings. Therefore, the mean collision frequencies are similar for the two incident-wave frequencies, with both  $0.14$ – $0.15$  Hz, i.e., collisions every  $6.7$ – $7.2$  s, and the corresponding mean collision velocities are

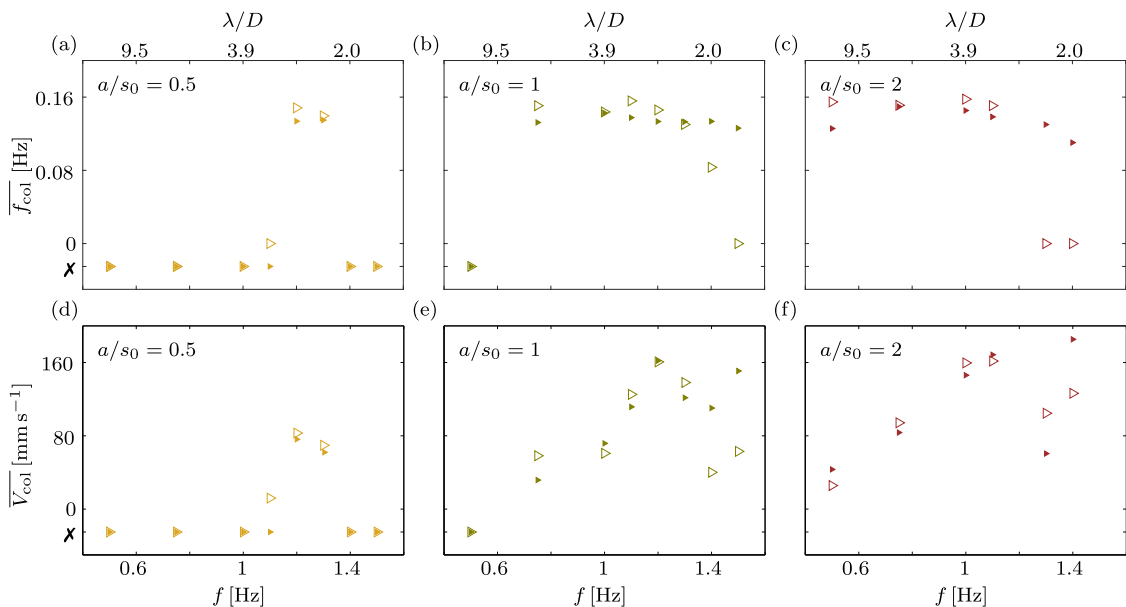


FIG. 11. Mean collision frequencies [(a)–(c)] and mean collision velocities [(d)–(f)], as functions of incident-wave frequency/non-dimensional wavelength, from experimental measurements (gold triangles, etc.) and model simulations (gold filled triangles, etc.). The  $\times$  symbol denotes no collisions in a test/simulation. Panels are grouped according to target wave amplitudes.

69.7–83.0 mm s<sup>-1</sup>. For  $f = 1.1$  Hz, a single weak collision occurs (behaviour III; transitory tests in Fig. 5) with collision velocity 12.0 mm s<sup>-1</sup>.

For the intermediate incident amplitude,  $a/s_0 = 1$ , multiple collisions occur for incident frequencies  $f = 0.75$ –1.4 Hz ( $\lambda/D = 2.0$ –6.7). Tests display behaviour II for  $f = 0.75$ –1.3 Hz, and the mean collision frequencies are 0.13–0.16 Hz, similar to those for the smallest incident amplitude. The corresponding mean collision velocities,  $\overline{V}_{\text{col}}$ , display greater variation, with maximum value 160.7 mm s<sup>-1</sup> for  $f = 1.2$  Hz and minimum 58.2 mm s<sup>-1</sup> for the lowest incident frequency where collisions occur,  $f = 0.75$  Hz. Only a small number of collisions occur for incident frequency  $f = 1.4$  Hz, and only a single collision occurs for  $f = 1.5$  Hz (behaviour III), and the corresponding mean collision velocities are significantly smaller than the lower frequencies, with  $\overline{V}_{\text{col}} = 40.1$ –63.0 mm s<sup>-1</sup>.

For the largest incident amplitude,  $a/s_0 = 2$ , multiple collisions occur for incident frequencies  $f = 0.5$ –1.1 Hz ( $\lambda/D = 3.9$ –12.3), with mean collision frequencies 0.15–0.16 Hz and tests displaying behaviour II. For  $f = 0.5$ –1 Hz, the mean collision velocity rapidly increases with increasing frequency, from 25.7 mm s<sup>-1</sup> at  $f = 0.5$  Hz to 159.6 mm s<sup>-1</sup> at  $f = 1$  Hz, as the collisions become more forceful due to greater relative surge (not shown). As the incident frequency increases to the largest two values,  $f = 1.3$  and 1.4 Hz, the tests transition to behaviour III more rapidly than for  $a/s_0 = 1$ , and only single, drift-driven collisions occur, as shown in Fig. 8. The corresponding collision velocities do not display a trend, noting that they represent velocities for single collisions only.

## B. Model–data comparison

For the smallest incident amplitude,  $a/s_0 = 0.5$ , the model captures the correct collision behaviours for all tests, except for incident frequency  $f = 1.1$  Hz, where it misses the single collision in the test by less than 1 mm, i.e., a collision almost occurs. However, the model does not simulate disk displacements accurately for the highest two frequencies,  $f = 1.4$  and 1.5 Hz (not shown). For incident frequencies where multiple collisions occur,  $f = 1.2$  and 1.3 Hz, the model predicts the mean collision frequency to within 9.8% and 3.4% of the respective measured frequencies and the mean collision velocity to within 8.1% and 11% of the respective measured velocities.

For the intermediate amplitude,  $a/s_0 = 1$ , the model predicts the mean collision frequencies and velocities accurately for incident frequencies  $f \leq 1.3$  Hz ( $\lambda/D \geq 2.3$ ), with a mean difference of 5.9% for collision frequency and 14.5% for velocity. For the largest amplitude,  $a/s_0 = 2$ , the model is accurate for  $f \leq 1.1$  Hz ( $\lambda/D \geq 3.2$ ), with average differences for collision frequency and velocity of 8.9% and 23.2%, respectively, noting that data were not obtained for  $f = 1.2$  Hz at this amplitude.

Model predictions are not accurate for high incident frequencies, with the range of frequencies increasing from  $f \geq 1.4$  Hz ( $\lambda/D \leq 2.0$ ) for  $a/s_0 = 1$  to  $f \geq 1.3$  Hz ( $\lambda/D \leq 2.3$ ) for  $a/s_0 = 2$  (again noting that the agreement for  $f = 1.2$  Hz is unknown). In the high incident frequency regime, more collisions occur in the simulations than the corresponding tests (hence larger mean collision frequencies) and the collisions

are generally more forceful in the simulations (hence larger mean collision velocities).

Figure 12 summarises the agreement between the mathematical model (based on slope-sliding theory and rigid-body collisions) and experimental data in non-dimensional amplitude–wavelength space, with the experimental collision behaviours indicated by the underlying colours, as in Fig. 5. Agreement is assessed in terms of (i) collision behaviours and (ii) disk displacements, where criterion (i) is evaluated according to the number of collisions (i.e., no collisions, 1–3 collisions, and >3 collisions) as defined in Sec. II D, and criterion (ii) is based on the general characteristics of disk displacements (i.e., similarities/differences in transient and steady-state displacements, separations, surge amplitudes, and drift).

The model accurately predicts the collision behaviours and disk displacements for intermediate–long incident wavelengths,  $\lambda/D > 2.3$ , for which tests display collision behaviours I and II (no collisions and regular, surge-driven collisions, respectively). For short incident wavelengths,  $\lambda/D < 2.3$ , and the smallest target incident amplitude,  $a/s_0 = 0.5$ , for which the tests display behaviour I, the model predicts the collision behaviours correctly, but not the disk displacements, as it does not capture the large drift experienced by the disks in the tests. For short incident wavelengths and the largest two target incident amplitudes,  $a/s_0 = 1$  and 2, for which tests display collision behaviour III (an initial drift-driven collision, quickly followed by up to two weak collisions, before the disks settle to a quasi-steady separation), the model does not predict the collision behaviour or the disk displacements. The model also does not accurately predict the collision behaviour for the transitory test with  $\lambda/D = 3.2$  and  $a/s_0 = 0.5$  (with behaviour III), although disk displacements are accurately simulated. As mentioned at the beginning of Sec. IV B, the disagreement in collision

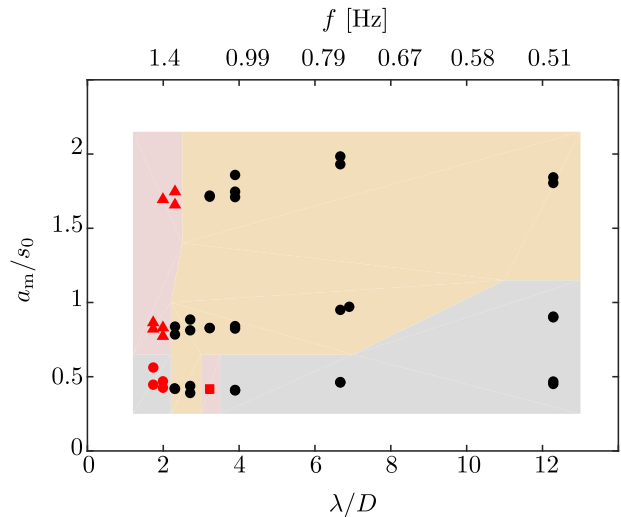


FIG. 12. Agreement between the mathematical model and experimental data in non-dimensional incident-wave amplitude–wavelength space: agreement in collision behaviours and disk displacements (black bullets); agreement in collision behaviours but not in displacements (red bullets); agreement in displacements but not in collision behaviours (red squares); and no agreement in collision behaviours and displacements (red triangles). Underlying colours divide amplitude–wavelength space into different experimental collision behaviours, as in Fig. 5.

behaviour is a result of the model narrowly missing a single weak collision in the test.

## V. EXTENDED MODEL

During the experiments, wave scattering between disks and disk drift along the tank were observed to regulate collision behaviours for short incident wavelengths (high incident frequencies; see Sec. II D). Equation of motion (5) does not model scattering forces, and Yiew (2017) shows that the drift it predicts due to sliding forces is up to two times less than the measured drift shown in Fig. 3(b). Therefore, the modified equation of motion

$$m(1 + c_m) \frac{d^2 X_j}{dt^2} = -mg \left[ \frac{\partial \eta}{\partial x} \right]_{x=X_j} + \rho c_d W |\widehat{V}_j| \widehat{V}_j - K \check{X}_j - CV_j + F_s + F_d \quad (14)$$

for  $j = 1, 2$ , where  $F_s(t)$  and  $F_d(t)$  are scattering and drift forces, respectively, is used for short incident wavelengths. The scattering and drift forces are modeled using the sigmoid functions

$$F_s(t) = \frac{(-1)^j M_s}{1 + e^{-\kappa(t-t_m)}} \quad \text{and} \quad F_d(t) = \frac{M_d}{1 + e^{-\kappa(t-t_m)}}, \quad (15)$$

thus increasing the forces from zero at the beginning of simulations to constant, maximum values,  $M_s > 0$  and  $M_d > 0$ , during the steady-state intervals. The scattering forces applied to disks 1 and 2 act in negative and positive  $x$ -directions, respectively, whereas the drift force acts in the positive  $x$ -direction for both disks. The time coordinate of the sigmoid curve inflection point  $t_m$  and the curve steepness  $\kappa$  are deduced from wave probe data, with  $\kappa \approx 10$  and  $t_m$  varying as a function of wave celerity. The maximum scattering force,  $M_s$ , is tuned to give accurate disk separations in the steady-state interval for tests with high incident frequencies ( $f = 1.4$  and  $1.5$  Hz for  $a/s_0 = 0.5$  and  $1$ , and  $f = 1.3$  and  $1.4$  Hz for  $a/s_0 = 2$ ). The maximum drift force,  $M_d$ , determines the mean steady-state displacements of the disks and is deduced from the single disk drift velocity shown in Fig. 3(b). For each test, the drift force,  $M_d$ , and the drag coefficient,  $c_d$ , are tuned such that (i) system (14) gives the required single disk drift velocity when  $K = C = M_s = 0$ , and (ii) the simulated mean steady-state displacements of the two-disk system agrees with data from the collision experiments. Following this criteria, drag coefficients between  $0.05$  and  $0.1$  were required for good model-data agreement in high incident frequency tests. These values are

noted to agree with those reported in Fig. 10(c) if the data were extrapolated.

Figure 13 shows disk displacements in two short incident wavelength tests, with corresponding displacements given by the basic model ( $F_s = F_d = 0$ ) and the extended model including scattering and drift ( $F_s = F_d \neq 0$ ). Figure 13(a) shows displacements for a test with  $\lambda/D = 2.0$  ( $f = 1.4$  Hz) and  $a/s_0 = 0.5$ , exhibiting behaviour I. The disks initially experience a drift force, which displaces the disks down the basin. The drift force, however, is relatively weak and is quickly overcome by restoring forces from the mooring, which cause the disks to settle to long-period oscillations around a mean separation of  $s = 34$  mm, which is slightly greater than the initial separation,  $s_0 = 20$  mm, due to weak scattering forces. By contrast, the basic model predicts virtually no drift and a mean separation equivalent to  $s_0$ . Using  $M_d = 0.005$  N and  $M_s = 0.002$  N, the extended model is able to capture the initial drift and mean separation.

Figure 13(b) shows displacements for a test with  $\lambda/D = 1.7$  ( $f = 1.5$  Hz) and  $a/s_0 = 1$  [also shown in Fig. 8(b)]. The scattering and drift forces are much larger than for the test shown in Fig. 13(a), resulting in the disks settling to a large mean separation  $s = 210$  mm, with the midpoint approximately  $300$  mm down the tank from its initial location, following an isolated initial collision (behaviour III). The basic model, with a large drag coefficient  $c_d = 1$ , predicts drift, but with the midpoint between the disks only  $180$  mm down the tank after  $t = 60$  s and the disks colliding repeatedly over this duration (behaviour II). The extended model uses relatively large values of the maximum drift and scattering forces,  $M_d = 0.085$  N and  $M_s = 0.03$  N, respectively, to capture the large displacement of the disks along the tank and their large mean separation, although it misses the initial collision due to small differences in the incident-wave forcing (hence behaviour I).

Figure 14 shows results for the test with  $\lambda/D = 2.0$  and  $a/s_0 = 1$ , for which the extended model is unable to capture the collisions and disk displacements due to sensitivities of the motions to irregularities in the incident wave. Figure 14(a) shows the incident-wave profile measured during the test and the fitted wave profile used in the model. As described in Sec. III A, the envelope of the fitted profile monotonically increases during the transient phase, before reaching a constant, maximum value in the steady-state interval. The fitted profile closely matches the measured profile, except around  $t = 10$  s where the measured amplitude spikes, reaching up to  $1.3$  times the steady-state amplitude. (The repetition of

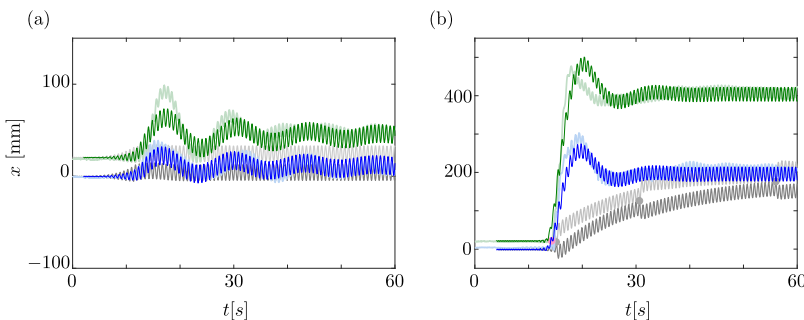


FIG. 13. Disk displacements and collisions measured during the experiments (shaded curves/bullets) and predicted by the basic model ( $F_s = F_d = 0$ , gray curves/bullets) and the extended model ( $F_s = F_d \neq 0$ , green and blue curves), for tests with (a)  $\lambda/D = 2.0$  and  $a/s_0 = 0.5$ , and (b)  $\lambda/D = 1.7$  and  $a/s_0 = 1$ .

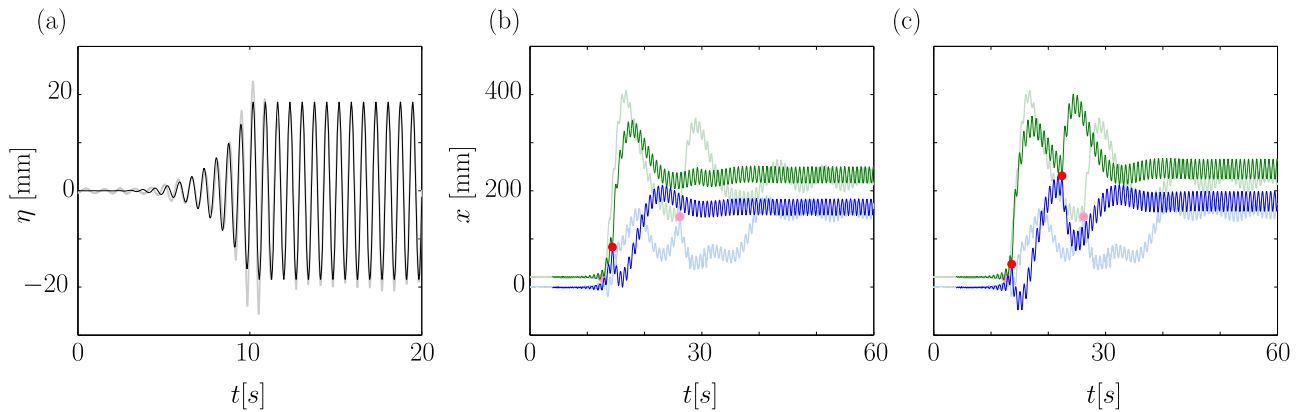


FIG. 14. (a) Measured incident-wave profile (gray curve) for test with  $\lambda/D = 2.0$  and  $a/s_0 = 1$ , and corresponding profile used in model (black curve). (b) Disk displacements and collisions predicted by the extended model (green/blue curves and red bullets) and measured during the experiment (shaded curves/bullets). (c) As in panel (b), but with incident amplitude used in the model is increased by a factor of 1.3 to match the maximum measured incident amplitude.

this test condition gave a near-identical wave profile and disk displacements.)

Figure 14(b) shows the corresponding disk displacements during the test and model simulation. In the test, the spike in the incident wave causes the disks to collide at a relatively early time. The disks then display irregular displacements, including a second, strong collision, before settling to a quasi-steady separation after  $t = 40$  s. The values  $M_d = 0.055$  N and  $M_s = 0.007$  N are used in the extended model to capture the steady-state behaviour, but the model predicts the first collision 1.8 s later than in the test, misses the second collision, and does not capture irregularity in the displacements, instead settling to the steady-state behaviour at the earlier time  $t = 32$  s.

Figure 14(c) shows the displacements when the steady-state amplitude in the model is increased by a factor of 1.3 so that it matches the maximum amplitude in the experiment. All other parameters remain consistent with Fig. 14(b). The increased amplitude brings the time at which the initial collision occurs closer to the test and produces more irregularity in the displacements, resulting in a second collision, similar to the test. However, the simulated displacements during the irregular, transient phase do not match the displacements well, and the steady-state displacements do not agree as well for the larger incident amplitude, e.g., the disks drift slightly farther along the tank in the simulations. Naturally, simulating a spike in the incident wave would improve the model–data agreement, but this would undermine the simple predictive capabilities of the model, and the case shown highlights potential sensitivities of collision and displacement behaviours in the short-wavelength regime.

## VI. CONCLUSIONS

Measurements of collisions between two thin floating disks forced by regular incident waves during laboratory wave basin experiments have been analysed. The tests covered incident wavelengths ranging from 1.7 to 12.2 times the disk diameter and incident amplitudes 0.5–2 times the initial disk separation. Dominant physical mechanisms influencing

collisions, such as surge, drift, and the relative phases between disks, were investigated over the range of incident-wave parameters. Three collision behaviours were identified: (I) disks do not collide for small incident amplitudes and short wavelengths because surge amplitudes and drift velocities are small, and long wavelengths because the disks surge in phase with one another; (II) disks collide repeatedly at regular periods in intermediate–long wavelengths (when wavelengths are approximately  $\geq 3$  times the disk diameter) over the entire range of wave amplitudes tested; and (III) disks initially collide several times and remain apart in the short-wavelength regime and in intermediate to large amplitude waves. It was shown that behaviour II can be predicted by using the surge motions of a solitary disk.

A mathematical model of the disk displacements and collisions was developed, based on slope-sliding theory for the displacements and rigid-body collisions. The drag coefficient appearing in the slope-sliding theory was tuned according to the experimental data, and it was found that it increases as incident wavelength decreases and incident amplitude increases. The model was shown to predict collision frequencies and velocities accurately for incident wavelengths greater than 2–3 times the disk diameter. For shorter wavelengths, wave scattering and drift forces were shown to influence disk displacements and collision behaviours. The model was extended to include these forces, and the extended model was shown to predict disk displacements, and hence collisions, far more accurately than the standard model. The accuracy of the model is more telling given that the model only considers a linear free-surface profile. The effect of free-surface nonlinearities remains an open problem, although, at present, there is insufficient evidence to suggest that including free-surface nonlinearities will significantly improve the model.

The model–data agreement implies that the model could act as a basis for modeling wave-induced collisions in a field of ice floes. In this respect, the present model is, of course, limited to the consideration of motions in a single horizontal direction only. More generally, this investigation is limited to the consideration of non-rafting collisions only.

## ACKNOWLEDGMENTS

The Australian Research Council funded the Ph.D. Scholarship of L.J.Y. The U.S. Office of Naval Research supports M.H.M. The Australian Maritime College funded the experiments. The authors thank Tim Lilienthal and Kirk Meyer for technical support during the experiments.

- Bennetts, L. G. and Williams, T. D., "Water wave transmission by an array of floating disks," *Proc. R. Soc. London, Ser. A* **471**, 20140698 (2015).
- Frankenstein, S., "The effects of waves on pancake ice," Ph.D. thesis, Clarkson University, 1996.
- Gao, L., "Ice floe collision under wave action in the marginal ice zone," M.S. thesis, Memorial University of Newfoundland, 1991.
- Grotmaack, R. and Meylan, M. H., "Wave forcing on small floating bodies," *J. Waterw. Port Coast. Ocean Eng.* **132**, 192–198 (2006).
- Herman, A., "Molecular-dynamics simulation of clustering processes in sea-ice floes," *Phys. Rev. E* **84**, 056104 (2011).
- Herman, A., "Influence of ice concentration and floe-size distribution on cluster formation in sea-ice floes," *Cent. Eur. J. Phys.* **10**(3), 715–722 (2012).
- Herman, A., "Numerical modeling of force and contact networks in fragmented sea ice," *Ann. Glaciol.* **54**(62), 114–120 (2013).
- Huang, G., Law, A. W. K., and Huang, Z., "Wave-induced drift of small floating objects in regular waves," *Ocean Eng.* **38**(4), 712–718 (2011).
- Marchenko, A. V., "The floating behaviour of a small body acted upon by a surface wave," *J. Appl. Math. Mech.* **63**(3), 471–478 (1999).
- Martin, S. and Becker, P., "High frequency ice floe collisions in the Greenland Sea during the 1984 marginal ice zone experiment," *J. Geophys. Res.* **92**(C7), 7071–7084, <https://doi.org/10.1029/jc092ic07p07071> (1987).
- Martin, S. and Becker, P., "Ice floe collisions and their relation to ice deformation in the Bering Sea during February 1983," *J. Geophys. Res.* **93**(C2), 1303–1315, <https://doi.org/10.1029/jc093ic02p01303> (1988).
- Masson, D. and LeBlond, P., "Spectral evolution of wind-generated surface gravity waves in a dispersed ice field," *J. Fluid Mech.* **202**, 43–81 (1989).
- McGovern, D. J. and Bai, W., "Experimental study on kinematics of sea ice floes in regular waves," *Cold Reg. Sci. Technol.* **103**, 15–30 (2014).
- McKenna, R. F. and Crocker, G. B., "Wave energy and floe collisions in marginal ice zones," in *Ice Technology for Polar Operations, Proceedings of the 2nd International Conference on Ice Technology* (Computational Mechanics Publications, Southampton, 1990), pp. 33–41.
- Meylan, M. H., Bennetts, L. G., Cavaliere, C., Alberello, A., and Toffoli, A., "Experimental and theoretical models of wave-induced flexure of a sea ice floe," *Phys. Fluids* **27**(4), 041704 (2015a).
- Meylan, M. H., Yiew, L. J., Bennetts, L. G., French, B. J., and Thomas, G. T., "Surge motion of an ice floe in waves: Comparison of theoretical and experimental models," *Ann. Glaciol.* **56**(69), 155–159 (2015b).
- Montiel, F., Bennetts, L. G., Squire, V. A., Bonnefoy, F., and Ferrant, P., "Hydroelastic response of floating elastic discs to regular waves. Part 2. Modal analysis," *J. Fluid Mech.* **723**, 629–652 (2013a).
- Montiel, F., Bonnefoy, F., Ferrant, P., Bennetts, L. G., Squire, V. A., and Marsault, P., "Hydroelastic response of floating elastic discs to regular waves. Part 1. Wave basin experiments," *J. Fluid Mech.* **723**, 604–628 (2013b).
- Rottier, P. J., "Floe pair interaction event rates in the marginal ice zone," *J. Geophys. Res.* **97**(C6), 9391–9400, <https://doi.org/10.1029/92jc00152> (1992).
- Rumer, R. R., Crissman, R. D., and Wake, A., *Ice Transport in Great Lakes* (Great Lakes Environmental Research Laboratory, National Oceanic and Atmospheric Administration, U.S. Department of Commerce, 1979).
- Shen, H. H. and Ackley, S. F., "A one-dimensional model for wave-induced ice-floe collisions," *Ann. Glaciol.* **15**, 87–95 (1991).
- Shen, H. H. and Squire, V. A., "Wave damping in compact pancake ice fields due to interactions between pancakes," in *Antarctic Sea Ice: Physical Processes, Interactions and Variability* (American Geophysical Union, Washington, D.C., 1998), Vol. 74, pp. 325–341.
- Yiew, L. J., "Modelling the wave-induced collisions of ice floes," Ph.D. thesis, University of Adelaide, 2017.
- Yiew, L. J., Bennetts, L. G., Meylan, M. H., French, B. J., and Thomas, G. A., "Hydrodynamic responses of a thin floating disk to regular waves," *Ocean Modell.* **97**, 52–64 (2016).